

UAV Icing: Experimental and Numerical Study of Glaze Ice Performance Penalties on an RG-15 Airfoil

Johannes Wolfgang Oswald*

University of Stuttgart, Stuttgart, D-70569, Germany

Norwegian University of Science and Technology, Trondheim, NO7491, Norway

von Karman Institute for Fluid Dynamics, Sint-Genesius-Rode, B-1640, Belgium

Adriana Enache†

von Karman Institute for Fluid Dynamics, Sint-Genesius-Rode, B-1640, Belgium

Université Libre de Bruxelles, Brussels, B-1050, Belgium

Richard Hann‡

Norwegian University of Science and Technology, Trondheim, NO7491, Norway

UBIQ Aerospace, Trondheim, NO7491, Norway

Gertjan Glabeke§

von Karman Institute for Fluid Dynamics, Sint-Genesius-Rode, B-1640, Belgium

Thorsten Lutz¶

University of Stuttgart, Stuttgart, D-70569, Germany

A key limitation to the operational envelope of medium-sized fixed-wing unmanned aerial vehicles (UAVs) today is the risk of atmospheric in-flight icing. This type of UAV has a wingspan of up to several meters and requires an all-weather capability for long-endurance and long-range missions. In contrast to the well-established icing issue in manned aviation, UAV icing is an emerging research topic. This paper aims to contribute to the ongoing validation of established numerical tools used for manned aviation. Their new arising use case are the one order of magnitude lower Reynolds number regimes of medium-sized fixed-wing UAVs. To achieve this, an experimental study with a 3D printed glaze ice shape inside the largest wind tunnel facility of the von Karman Institute in Belgium is conducted. The glaze ice shape is obtained from previous icing wind tunnel experiments. Furthermore, a numerical CFD study of the experiments with the FENSAP flow solver module of ANSYS FENSAP-ICE is performed. A final comparison of both experimental and numerical results is conducted to evaluate the glaze ice induced aerodynamic performance penalties on a clean RG-15 airfoil. The results are indicating that the chosen one-equation Spalart-Allmaras turbulence model has limited capabilities of capturing the onset of stall behaviour and achievable maximum lift of the clean and artificially glaze iced RG-15 airfoil. Nevertheless, the Spalart-Allmaras turbulence model is in general able to predict the order of the induced drag and moment penalties.

I. Introduction

Forecasts of unmanned aerial vehicle (UAV) market growth rates may differ in numbers, but are overall agreeing on predicting an annual growth rate between 10% and 25% from 2014 to 2025 [1, 2]. An in the year 2019 published report from the Federal Aviation Administration (FAA) [1] reveals that the commercial non-model aircraft market is estimated

*Research Associate and PhD Student, Institute of Space Systems, Pfaffenwaldring 29, johannes.wolfgang.oswald@gmail.com

†PhD Candidate, Environmental and Applied Fluid Dynamics Department, Waterloosesteenweg 72, Aero-Thermo-Mechanics Department, Avenue F.D. Roosevelt 50, adriana.enache@vki.ac.be

‡Researcher, Centre for Autonomous Marine Operations and Systems (AMOS), Department of Engineering Cybernetics, UAV Icing Lab, NTNU, O.S. Bragstads plass 2D, richard.hann@ntnu.no, corresponding author

§Senior Test Engineer, Waterloosesteenweg 72, glabeke@vki.ac.be

¶Researcher and Head of working group Aircraft Aerodynamics and Wind Energy, Institute of Aerodynamics und Gas Dynamics, Pfaffenwaldring 21, lutz@iag.uni-stuttgart.de

to triple from 277 000 units in 2018 up to 835 000 in 2023. The market-driving conceivable future applications are e.g. blood deliveries to hospitals, commercial package deliveries, and search-and-rescue operations [1, 3]. However, these future applications are currently limited by e.g. battery life and safety, as well as by un-clarified flight regulations and authorisations from the national institutions. Besides these technical and regulatory limitations, another key limitation to the operational envelope of UAVs today is the risk of atmospheric in-flight icing [4].

In flight-icing of an UAV (or any other aircraft) is the accretion process of freezing liquid droplets, when they are impinging onto the UAV fuselage, propeller, sensors, etc. The UAV is prone to in-flight icing, when the flightpath is passing through clouds or precipitations [4]. The icing environment is characterized by the ambient temperature and the airspeed [5]. However, for defining the accreting ice topology, the liquid water content, the droplet size and the accretion time are playing also an important role [5]. Icing conditions are in general achieved inside supercooled liquid droplet clouds, so called freezing clouds. Within these freezing clouds, different ice shape morphologies can form on lifting surfaces (e.g. wings): glaze, rime, and mixed ice [6]. A fourth ice shape accretion, which occurs more rarely, is taking place in freezing precipitations and is characterized by supercooled large droplets [5]. Detailed information about the ice accretion process and the different ice shapes can be found in [4–6].

A recently published climate report for Norway and the Nordics from UBIQ Aerospace [7] highlights and quantifies the in-flight icing risks of UAVs today: In the winter months, the highly affected altitudes are from ground up to 3 000 m. In the summer months, the risk of atmospheric in-flight icing remains at a significant level up to the typical UAV maximum operating altitude of 6 000 m [7]. Consequently, especially long-endurance and long-range UAVs are requiring an all weather capability [8]. Following on, this all weather capability requirement motivates ice protection technologies for UAVs like the "D•ICE" system by UBIQ Aerospace [9]. Since the existing icing simulation tools are validated for manned aviation which operates typically at Reynolds numbers one order of magnitude higher than UAVs [8], the enabling of ice protection technologies for UAVs still requires validation of the numerical methods onto the low Reynolds number UAV-applications as recommended by Hann and Johansen [4]. This is also motivated by numerical studies showing a strong Reynolds number dependency of the ice accretion process [10–13].

The major goal of this paper is to provide experimental data on aerodynamic penalties induced by a typical glaze ice shape on a common airfoil of a medium-sized fixed-wing UAV with a wing span of several meters at the Reynolds numbers 200 000 and 400 000. Furthermore, this paper aims to also contribute to the ongoing validation of the manned aviation numerical tools for UAV applications. This is why the conducted experiments with a clean RG-15 airfoil and a three-dimensional (3D) printed glaze ice shape are compared to numerical computational fluid dynamics (CFD) simulations performed with the flow solver module of FENSAP-ICE. The experiments were conducted at the von Karman Institute for Fluid Dynamics (VKI) in Rhode-Saint-Genèse, Belgium and scientifically accompanied by its Environmental and Applied Fluid Dynamics Department, as well as by the Department of Engineering Cybernetics of the Norwegian University of Science and Technology (NTNU) in Trondheim, Norway, and by the Institute of Aerodynamics and Gas Dynamics (IAG) of the University of Stuttgart in Vaihingen, Germany.

II. Methodology

The wind tunnel facility L1-B of the VKI has the ability to conduct open and closed test section experiments by laterally exchanging the whole test section (see Fig. 1). For this paper the rectangular closed test section configuration is chosen with the geometrical dimensions of 2 m height, 3 m width, and 20 m length. This section contains two test beds of which the frontal one was used. The frontal test bed is equipped with a six component platform balance for aerodynamic force measurements. The tunnel is powered with a 580 kW direct current motor driving two contra-rotating fans providing a maximum achievable wind speed of $v = 25$ m/s for the testing campaign [14]. Therefore, the maximum Mach number of 0.07 yields incompressible flow conditions inside the wind tunnel and the Reynolds number was the relevant similarity parameter. Within the closed test section, the typical turbulence intensity level at $v = 20$ m/s was estimated by previous VKI internal studies to be around 0.8%.

The RG-15 Airfoil model When it comes to research concerning UAV in-flight icing, one of the most commonly used airfoil type is the RG-15, which was designed for high lift to drag (L/D) ratios at low Reynolds numbers by Rolf Girsberger [15]. It is a standard airfoil for radio controlled model sailplanes and has a relative thickness of 8.92% and a camber of 1.76%. The RG-15 is also used for small to mid-sized fixed-wing UAVs like the Maritime Robotics PX-31 "Falk" [16] designed for long-range and long-endurance missions, whose operational envelope requires an all-weather capability.

The coordinate data of the RG-15 was retrieved from [17]. The wing with a span-width of $b = 650$ mm, a chord

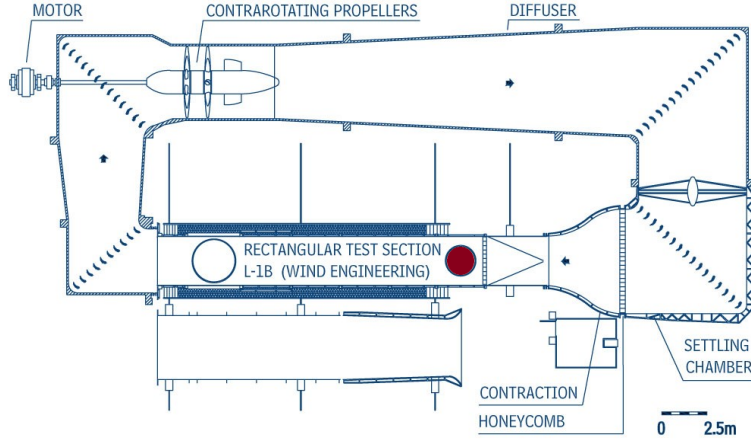


Fig. 1 Top down view of the L1-B testing facility at the VKI. The red dot indicates the frontal test bed location. At this position, the wind tunnel wing model was installed on top of test bed's six component platform balance.

length of $c = 450$ mm, and a trailing edge height of 2.4 mm was manufactured by Smart Solutions KP from Poland. It basically consists of a resin and glass fibre composite with a smooth grey surface finish. The wing was equipped with 23 connected pressure holes per side to enable pressure measurements along the wing's surface in chord direction.

The geometrical deviation of the manufactured wing model from the ideal RG-15 profile is shown in Fig. 2. The displayed RG-15C profile was generated on the basis of the ideal RG-15 airfoil with the software XFLR5 version 6.48 [18] to digitally resemble the wind tunnel wing model. A 2D flow analysis of the RG-15C and the wind tunnel wing model revealed their geometric difference to be negligible.

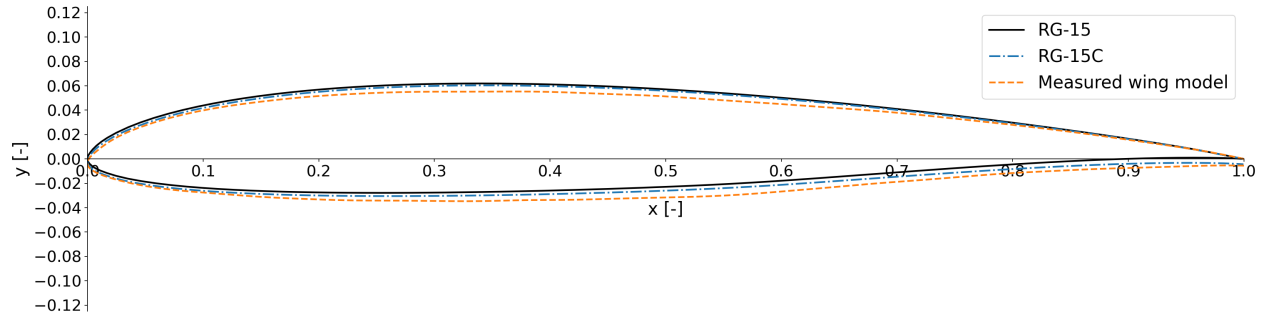


Fig. 2 Comparison of the RG-15 profile (black) to the measured profile contour (orange) of the tested wing in normalized coordinates. The normalized RG-15C (blue) with an open trailing edge of 0.44% chord was achieved based on the RG-15 with a blending distance from the trailing edge of 80% chord.

To achieve a purely two dimensional flow, a custom 2D wind tunnel section was constructed inside the L1-B wind tunnel. This reduced the effective wind tunnel cross section from 6 m^2 down to 1.32 m^2 . Between the wing model and the custom 2D wind tunnel walls remained a gap of 3 mm. Therefore, a physical decoupling of both elements was ensured.

3D-printed ice shapes During the experimental campaign a 3D-printed glaze ice shape was tested to gain more insight on the aerodynamic penalties resulting from atmospheric in-flight icing of mid-sized fixed-wing UAVs. The glaze ice topology was obtained by the NTNU during previous ice accretion experiments on an RG-15 airfoil inside an icing wind tunnel [5]. The tunnel facilities belong to the Technical Research Center in Finland (VTT) [19]. Details on the utilized liquid water content LWC , median droplet volume diameter MVD , accretion temperature T_{acc} and accretion time t_{acc} are provided in Tab. 1. The glaze ice shape was simplified to a 2D-cut of the accreted ice shape and extruded to the full span-width of the wing. The contour of the utilized ice shape is displayed in Fig. 3. With the aid of duct tape, the glaze ice shape was fixed in place at the leading edge of the wing (see Fig. 4).

Table 1 Icing conditions inside the VTT icing wind tunnel at the NTNU.

condition	$AoA [^\circ]$	v [m/s]	T_{acc} [°C]	t_{acc} [min]	LWC [g/m ³]	MVD [μ m]
Glaze	0	25	-2	20	0.44	26

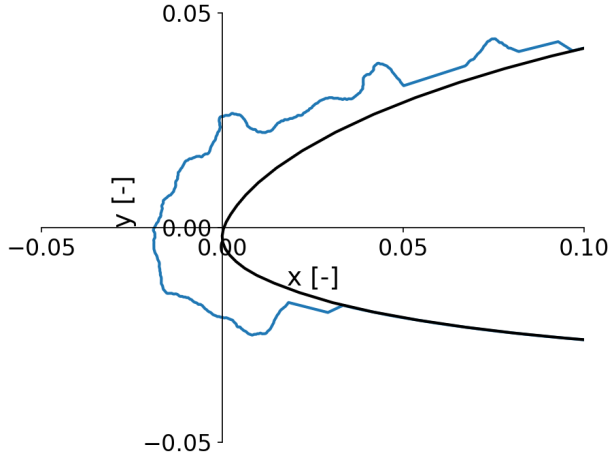


Fig. 3 Contour plot of the utilized 2D glaze ice cut (blue)

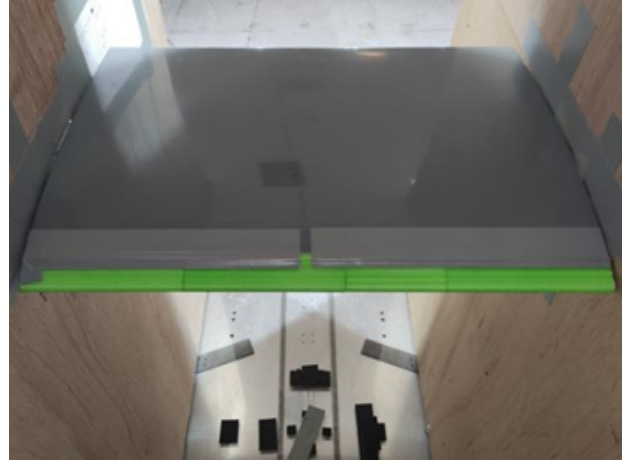


Fig. 4 3D-printed glaze ice shape mounted at the leading edge of the wing with the aid of duct tape and spared out pressure holes in the middle of the wing.

Parametric study approach Since the experiments inside the L1-B were conducted in incompressible flow regimes, the Reynolds number was a major similarity parameter. Two Reynolds number regimes were tested: The lowest Reynolds number was set to 200 000 to enable the comparison and validation to other conducted clean RG-15 airfoil wind tunnel tests from literature. Due to safety reasons regarding the expected maximum forces and moments on the wing model, the second Reynolds number was chosen to be 400 000. According to Eq. 1 this yields with a local density of $\rho = 1.213\ 3\text{ kg/m}^3$, the chord length as characteristic length of $c = 0.45\text{ m}$, and a dynamic viscosity of $\mu = 1.786\ 2 \times 10^{-5}\text{ kg/(m s)}$, free stream velocities of $v_\infty = 6.5\text{ m/s}$ and $v_\infty = 13.1\text{ m/s}$ respectively.

$$Re = \frac{\rho c v_\infty}{\mu} \quad (1)$$

Due to a limited testing time, the angular resolution was set to 3° , ranging from $AoA = -7.8^\circ$ until 13.2° with a 1° resolution near the stall region for the clean airfoil. The glaze ice shape was tested up to 10° . To investigate hysteresis effects, a second run was performed per velocity in an ascend-descend pattern. The hysteresis effects turned out to be negligible. The pressure and force measurements were acquired simultaneously as soon as static flow conditions were achieved.

Measurement equipment The six component platform balance in the frontal test bed of the L1-B wind tunnel was used to measure the aerodynamic forces and moments acting on the RG-15 wing model. The amplification gain of its data acquisition system was set to 2000 times the raw signal and the low pass filter was configured to a 200 Hz cut-off frequency, since no higher frequencies were expected for the measurements. The sampling frequency was set to 2 000 Hz, which results in 90 000 samples throughout the acquisition time of 45 s.

The platform balance was calibrated with the aid of a calibration rig and the calibration reference point was set as close to the RG-15 wing model mounting axis as possible with the aid of a 1m high calibration head. With the data from the calibration, it was possible to estimate the relative precision $\Delta\eta_i$ and accuracy $\Delta\varsigma_i$ of the balance's force and moment measurements. Both values are tabulated for each load component in Tab. 2. More details can be found in [20].

Furthermore, the airfoil was equipped with 46 pressure tabs connected to a pressure box with 48 digital pressure sensors underneath the wind tunnel. The two spare pressure channels of the box were used to measure the total pressure and the differential connected dynamic pressure of the Pitot-static probe placed upstream of the wing to determine the

Table 2 Imposed ranges, precision and accuracy of the balance calibration for each force and moment component.

Channel	Imposed range	Precision $\Delta\eta$	Accuracy $\Delta\varsigma$
Lift force	$\pm 107.75 \text{ N}$	0.88%	0.16%
Drag force	$\pm 9.55 \text{ N}$	1.37%	0.89%
Side force	$\pm 1.08 \text{ N}$	0.85%	3.23%
Roll moment	$\pm 1.96 \text{ N m}$	0.07%	4.09%
Pitch moment	$\pm 1.96 \text{ N m}$	0.76%	4.13%
Yaw moment	$\pm 1.96 \text{ N m}$	0.61%	1.12%

free stream velocity. All the pressure measurements were conducted with sensors of the AMS5812 series. The sampling frequency was set to 200 Hz, which yields a total number of 9 000 samples per 45 s of each test's acquisition time.

The pressure sensors with ranges lower than 4 000 Pa were calibrated with the aid of a water manometer and the higher pressure range sensors were calibrated by a DPI 610 pneumatic calibrator pump. The sensor types and ranges used for this paper, as well as their individual manufacturing accuracy $\Delta\xi_{\text{AMS5812}}$ and induced error by the calibration devices $\Delta\xi_{\text{calibration}}$, are provided in Tab. 3.

Table 3 Calculated accuracies of the utilized AMS5812 pressure sensors and their calibration device. The sensors below a range of 4 000 Pa were calibrated with a water manometer. For ranges greater 4 000 Pa, a DPI 610 pneumatic calibrator pump was used for calibration, which has an accuracy of 0.025% of their different pressure sensor ranges.

Regime	Type	Range [Pa]	$\Delta\xi_{\text{AMS5812}} [\text{Pa}]$	$\Delta\xi_{\text{calibration}} [\text{Pa}]$
Ultra low pressures	0000-D	0...517	± 3.88	± 0.98
	0000-D-B	± 517	± 7.76	± 0.98
	0001-D-B	$\pm 1\,034$	± 15.51	± 0.98
Low pressures	0003-D	0...2 068	± 10.34	± 0.98
	0015-D	0...10 342	± 51.71	± 5.00
	0008-D-B	$\pm 5\,516$	± 55.16	± 3.50
Standard pressures	0030-D	0...20 684	± 51.71	± 8.75
	0050-D	0...34 474	± 86.18	± 8.75
	0150-A	0...103 421	± 452.46	± 3.50
	0300-A	0...206 843	± 904.93	± 87.50

Uncertainty analysis and applied corrections A standard approach to estimate the uncertainties was applied according to [21]: The uncertainty of a function, which consists of multiple measured variables, is determined by extending the Pythagoras' law to cover each variables error contribution. These are calculated as the squared derivatives with respect to the single variable multiplied by the squared total error or uncertainty of the same variable. Building the square root out of the summed up products defines the uncertainty of the initial function [21]. A detailed analysis of the uncertainties of the experimental campaign can be found in [20].

Due to the fact, that the wing model's rotation axis was not aligned with the quarter point of its chord, the measured pitching moment $M_{\text{pitch}'}$ must be corrected according to

$$M_{\text{pitch}_{0.25}} = M_{\text{pitch}'} + L'l \sin(\alpha) + D'l \cos(\alpha) \quad (2)$$

where l is the distance between the axis centre and the wing's quarter point, α is the AoA, L' and D' are the measured lift and drag forces and $M_{\text{pitch}_{0.25}}$ is the corrected pitching moment. The distance was measured to $l = 78.2 \text{ mm}$.

The AoA alignment paper 0° indication line was coinciding with the chord of the wing. Therefore, the AoA was corrected to $\alpha = \alpha - 1.3^\circ$ because the wing rotation axis centre was slightly below the chord.

With respect to the 2D wall flow interferences e.g. the solid blockage leading to a velocity increase by continuity and Bernoulli's equation [22], the theoretical tunnel-wall corrections from Allen and Vincenti [23] were applied. They generally compensate for the effects of the compressibility of the fluid and the wake of the airfoil in a closed 2D test section. These corrections are valid for small chord c to tunnel height h ratios, which is the case for the conducted experiments $c/h = 0.225$. A detailed discussion of the applied corrections is presented in [20].

Numerical analysis methods One of the goals of this paper is to compare the experimental data on performance penalties on a typical UAV airfoil for low Reynolds numbers introduced by a 3D-printed glaze ice shape to numerical simulations. Therefore, the FENSAP flow solver module of ANSYS FENSAP-ICE 2021 R1 was used to conduct the CFD simulations [24, 25]. The FENSAP module utilizes Reynolds-averaged Navier-Stokes equation (RANS) fluid simulations.

The grid generation was done according to the proposed grid parameters set by Fajt et al. [13]. Among other things, these parameters were validated by Fajt et al. with a grid independence study. Pointwise V18.4R3 [26] was selected as the CFD mesh generation software. Herein, the T-Rex meshing algorithm allowed to rapidly generate the hybrid meshes.

Fajt et al. [13] investigated both, the numerical ice accretion with FENSAP-ICE and the aerodynamic performance penalties introduced by the numerically predicted ice shapes. Since the Reynolds number regimes, the ice shapes, and the airfoil geometry of Fajt et al. are similar to the ones' used in this paper, his validated grid parameters were adapted.

The grid parameters of the RG-15C hybrid O-grid are summarized in Tab. 4. Figures 5a – c are illustrating the discretised RG-15C. The hybrid O-grid needed to be extruded by one step in span-wise direction to retrieve a 2D mesh suitable for the FENSAP steady-state CFD calculations.

Table 4 RG-15C grid parameters.

Parameter	Setting
Dimension	2D
Airfoil discretization	160 points for lower and upper airfoil side, tanh-distributed, 8 points for trailing edge equally distributed
Chord length	$c = 0.45\text{ m}$
Initial cell height	$\Delta s = 1.0\text{ }\mu\text{m}$
Boundary layer discretization	Minimum of 1 full structured layer
Growth rate of structured layers	1.1
Circular far field discretization	140 points equally distributed and unstructured triangular cells
Circular far field diameter	$66.7c = 30\text{ m}$
Grid decay	0.9
Number of cells	$\approx 80\,000$

Ice shape grid The ice shape grid of the glaze ice was discretised with a constant spacing of 0.1 mm. The uncovered upper and lower airfoil surfaces were again discretised by 160 tanh-distributed points. A close-up of the leading edge region is provided by Fig. 5d.

Physical modelling of the ANSYS FENSAP module The ANSYS FENSAP module RANS fluid simulation settings are provided in Tab. 5. The turbulence modelling of the clean airfoil and ice-shape grids were conducted with the Spalart-Allmaras turbulence model, as according to Chung and Addy [27] it is recommended for icing simulations in manned aircraft. In the clean airfoil case, the transition from laminar to turbulent flow was prescribed with fixed locations. These locations were calculated with the aid of XFOIL [28]. On this occasion, the estimated 0.8% turbulence intensity inside the L1-B wind tunnel was accounted for by altering the standard value of the XFOIL's envelope e^n transition criterion [28] from its standard value $n = 9$ to $n = 3.15$. In the glaze ice case, it was assumed that no transition

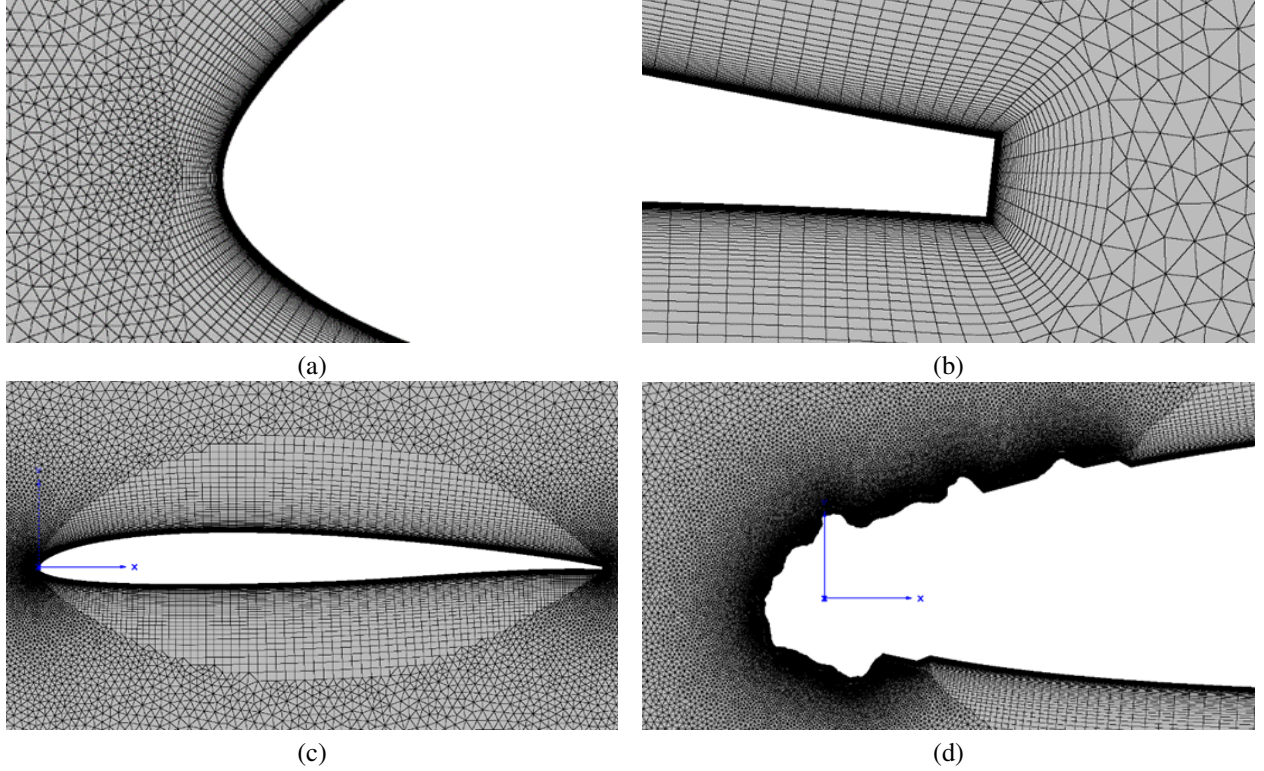


Fig. 5 Detail of the leading edge (a) and trailing edge (b) RG-15C hybrid O-grid. (c) illustrates the structured boundary layer and unstructured far field discretization and (d) shows a close-up of the glaze ice shape grid.

of laminar to turbulent flow occurs, since the ice shape surface roughness and topology causes the boundary layer to instantaneously trip.

Table 5 ANSYS FENSAP module CFD simulation settings.

Parameter	Setting
Turbulence model	Spalart-Allmaras
Transition clean RG-15C	Fixed transition locations
Transition iced RG-15C	No transition / fully turbulent boundary layer
Artificial viscosity	1×10^{-7}
CFL number	900
Number of time steps	5 000

III. Results

The experimental results are presented within polar plots in which the uncertainties are indicated per data point with error bars in the same colour as the test case. The numerical simulation results are afterwards compared to the experiments in terms of the coinciding of the aerodynamic and pressure coefficient propagation.

As shown in Fig. 6 and 7, the glaze ice shape mounted onto the leading edge of the RG-15 wind tunnel wing model induces considerable aerodynamic penalties to the baseline of the clean RG-15 airfoil. For example, at the tested Reynolds numbers of 200 000 and 400 000, the baseline drag coefficient is significantly increased at all tested AoA by the glaze ice shape (see Fig. 6b and 7b). At the Reynolds number of 200 000, the minimum drag coefficient of the clean RG-15 wind tunnel wing model is increased by the glaze ice shape by $\approx +40\%$. The reduction of the achievable lift at

the minimum drag coefficient varies between -20% and -50% (see Fig. 6a and 7a). Nevertheless, the glaze ice shape seems to not significantly influence the slope of the lift coefficient.

It is also evident from Fig. 6a and 7a, that for the glaze ice case deep stall conditions are not achieved at both tested Reynolds numbers. But the drag and moment coefficient plots indicate the onset of stall with a rapid increase of c_d and a moment break down of the c_m to more negative values at the highest tested AoA. In both Reynolds number cases, the glaze ice causes an destabilizing "nose-down" moment (see Fig. 6c and 7c).

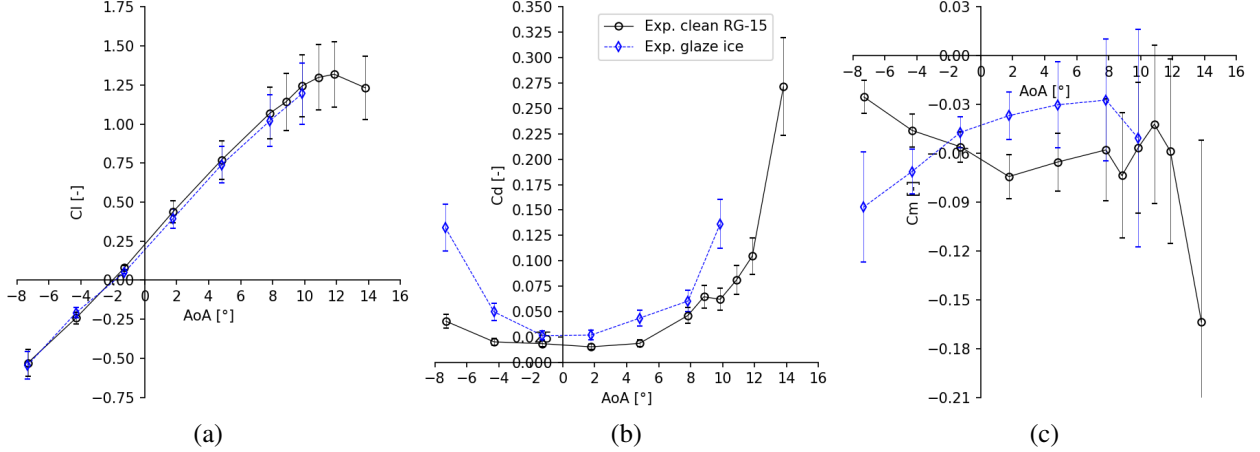


Fig. 6 Polar plots of lift coefficient c_l (a), drag coefficient c_d (b), moment coefficient c_m (c) over angle of attack AoA of the experimental campaign at $Re = 200\,000$.

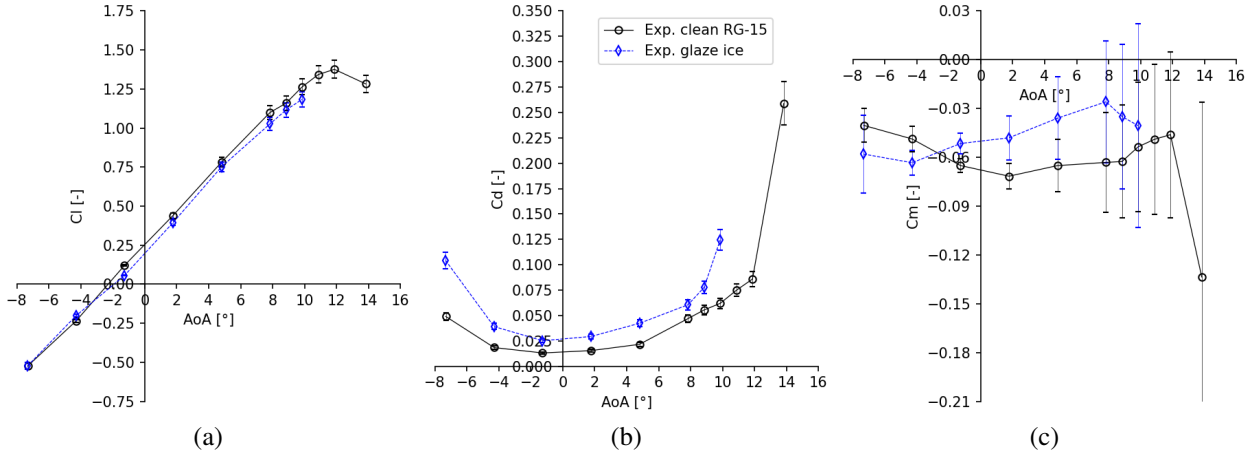


Fig. 7 Polar plots of lift coefficient c_l (a), drag coefficient c_d (b), moment coefficient c_m (c) over angle of attack AoA of the experimental campaign at $Re = 400\,000$.

Validation of the RG-15C grid with literature The validation of the RG-15C grid was conducted at a Reynolds number of 200 000 by comparing the FENSAP aerodynamic coefficient predictions with literature data from Selig et al. [15], Sartorius [29] and Rozehnal, whose experiments were conducted during the wind tunnel experiments of Lutz et al. [30]. Starting with the c_l over AoA diagram from Fig. 8a, FENSAP is in good agreement with the literature lift levels in between -8° and 6° . Above 6° , the FENSAP calculation estimates a higher $c_{l,\max}$ and an earlier onset of stall in comparison to the data from Rozehnal [30]. However, the c_d levels predicted by FENSAP and the experimental c_d values are alike (see Fig. 8b).

It was concluded that the RG-15C grid and the chosen Spalart-Allmaras turbulence model in combination with fixed transition locations were capable of adequately predicting the experimental clean airfoil data from literature but special care must be taken when evaluating the onset of stall.

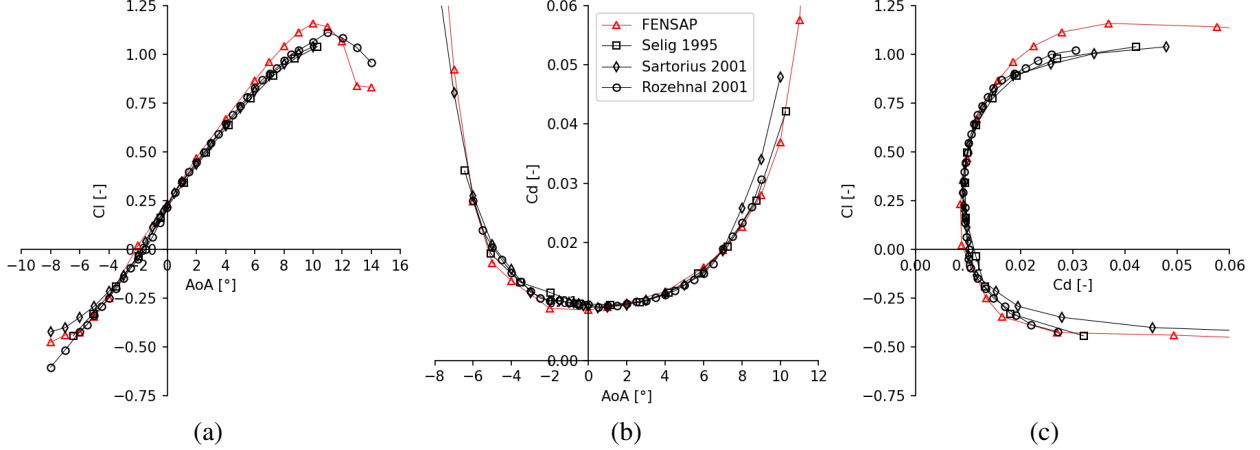


Fig. 8 Polar plots of lift coefficient c_l over angle of attack AoA (a), drag coefficient c_d over angle of attack AoA (b), drag polar (c) FENSAP prediction validation with multiple experimental data for the RG-15 at $Re = 200\,000$.

Comparison of the numerical and the experimental aerodynamic coefficient results The ANSYS FENSAP module CFD simulations of the 3D-printed glaze ice shape were conducted with a resolution of 1° between $AoA = -8^\circ$ and $AoA = 14^\circ$. The Figures 9 and 10 are displaying the aerodynamic coefficients over the AoA from the experimental and numerical results at the two investigated Reynolds numbers. As a general observation in the c_l over AoA plots, the slope of the lift coefficient is well captured by the simulations.

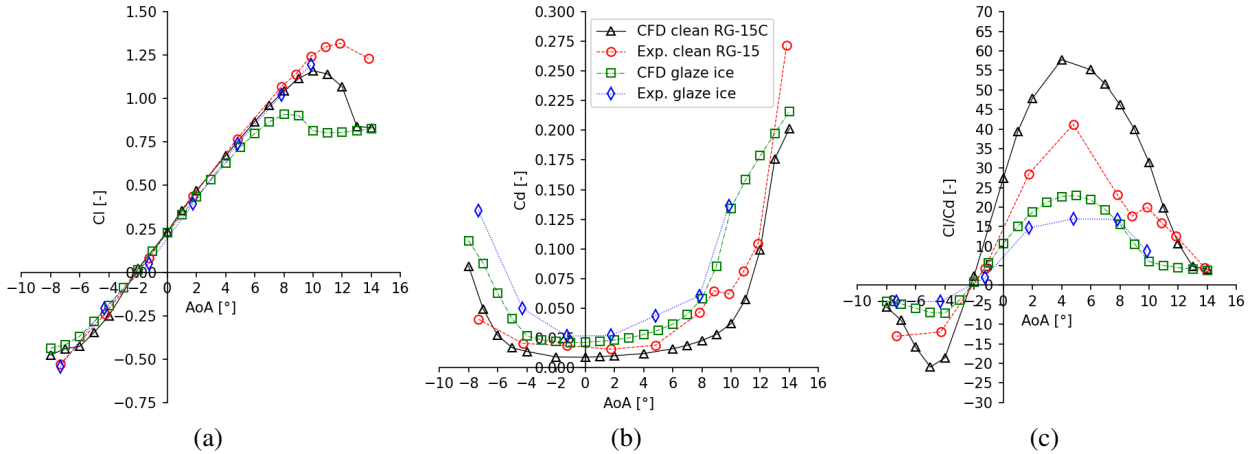


Fig. 9 Clean and glaze ice case comparison at $Re = 200\,000$ of lift coefficient c_l (a), drag coefficient c_d (b) and lift to drag ratio c_l/c_d (c) over angle of attack AoA of the FENSAP prediction and the experimental results.

The glaze ice experiments were not conducted until deep stall. However, the CFD simulations show a clear deficiency in predicting the onset off stall: For example, in Fig. 9a the glaze ice simulation is already stalled at $AoA = 9^\circ$, while the experimental glaze ice shows only the indications for the onset of stall at an $AoA = 9.8^\circ$ and records at the same AoA a 32% higher lift coefficient. This is similar to the Reynolds number of 400 000 (see Fig. 10a). Also, regarding the clean airfoil, the Spalart-Allmaras turbulence model seems to encounter problems in adequately predicting the onset of stall. Herein, the prediction of the CFD simulations is better, the higher the Reynolds number is. This is not a surprising result since the Spalart-Allmaras turbulence model was developed for applications of the manned aviation with one order of magnitude higher Reynolds number regimes than the UAV applications.

The drag coefficient of the clean airfoil experiments records for each Reynolds number significant higher levels as compared to the CFD simulations and literature data. This is especially the case for $AoA > 4.8^\circ$ (see Fig. 9b and 10b). However, the underlying phenomena seems to be less severe with the glaze ice shape mounted to the leading edge of the wing model since the drag coefficient penalties of the experimental glaze ice were higher than the more conservative

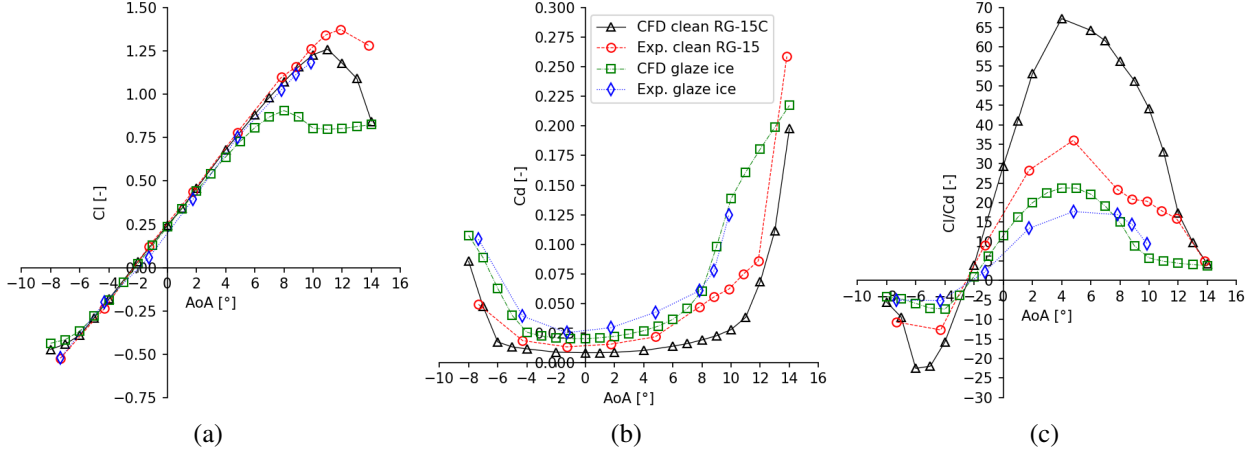


Fig. 10 Clean and glaze ice case comparison at $Re = 400\,000$ of lift coefficient c_l (a), drag coefficient c_d (b) and lift to drag ratio c_l/c_d (c) over angle of attack AoA of the FENSAP prediction and the experimental results.

FENSAP predictions, but in general captured. A possible explanation for the observed drag increase is presented in the discussion.

Comparison of the numerical and the experimental pressure coefficient results At the tested Reynolds numbers of 200 000 and 400 000 the pressure coefficient uncertainties are too high for the AMS5812 Standard Pressure sensors to allow a reasonable pressure analysis of the affected pressure tap locations (see Fig. 11). The affected pressure taps were located on the upper airfoil side (US) between the leading edge and $0.55c$ and on the lower airfoil side (LS) at the first and sixth position. Since the measured local static pressure was not exceeding 20 Pa at Reynolds numbers of 200 000 and 150 Pa at 400 000, the bias error of the AMS5812 Standard Pressure sensors were up to 45 times greater. Consequently, the pressure coefficient uncertainties are dominated by the bias error of the AMS5812 Standard Pressure sensors, as the manufacturing accuracy estimation of these sensors is given as a full-scale percentage. This is why the pressure tap locations of the US until $0.55c$ were only considered as a general pressure trend.

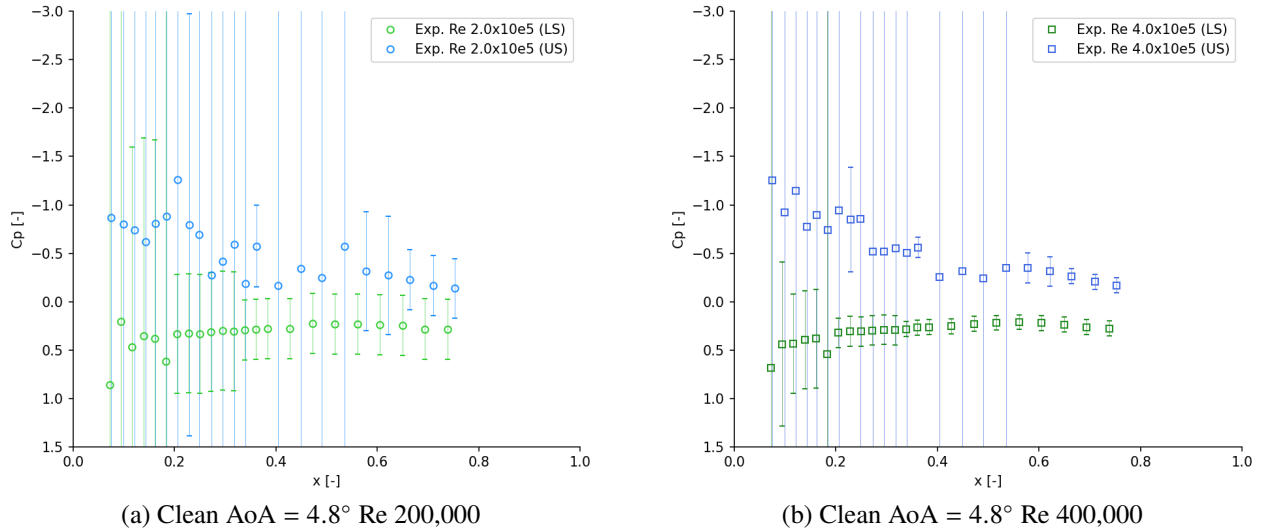


Fig. 11 Exemplary clean airfoil pressure coefficient c_p over dimensionless chord location x with uncertainty displayed as error bars at the Reynolds numbers 200 000 (a) and 400 000 (b).

The LS pressure taps experienced much lower uncertainties, which allowed a comparison of the experiments to the CFD results. The comparison revealed overall more positive c_p on the experimental side (see Fig. 13). The offset is

similar for all positive AoA and the c_p exceeds the value of 1 in the leading edge region of the LS. According to the definition of the pressure coefficient for incompressible flows, a $c_p = 1$ shows that the local static pressure is equal to the stagnation pressure of the airflow. Consequently, the local static pressure at the airfoil was higher than the one measured by the Pitot-static probe placed upstream of the constructed 2D wind tunnel inside the larger L1-B wind tunnel test section. This implies a higher free stream velocity at the airfoil position.

The predicted clean airfoil pressure coefficient distributions between $-7.3^\circ < \text{AoA} < 9.8^\circ$ of the CFD simulations are in good agreement with the experimentally retrieved values (see Fig. 12a, c, e, and Fig. 13a, c, e).

Similar to the clean airfoil experiments, the glaze ice c_p plots were exceeding more positive c_p levels at the LS compared to the CFD simulation (see Fig. 12b, d, f, and Fig. 13b, d, f). This was also correlated to the presence of an higher free stream velocity at the airfoil position than measured by the Pitot-static probe ahead of the constructed 2D-wind tunnel inside the L1-B.

The onset of a separation bubble indicating pressure plateau [31] is visible on the US of Fig. 13d and f at $x < 0.4$. This is in good coincidence with the aerodynamic coefficient plots, where in the glaze ice case the a rapid c_p raise and c_m reverse sweep to more negative values is observable at similar AoA (see Fig. 6b, c, and Fig. 7b, c). This trend is not observable in the FENSAP simulations.

IV. Discussion

The conclusions of the comparisons are summarized and critically evaluated regarding the chosen numerical methodology. Furthermore, the rapid drag increase of the clean airfoil experiments at higher AoA are addressed and explanations for the observed flow phenomena are provided in the course of this discussion.

Influence of the Reynolds number Figure 14 displays the experimental results of the artificial glaze iced and clean RG-15 aerodynamic coefficients at multiple Reynolds numbers. The displayed results for the airfoil with the glaze ice show no significant deviations of the drag polars between the Reynolds numbers of 200 000 and 400 000 at positive AoA (see Fig. 14a). A difference between the aerodynamic performance of the glaze ice shape at the Reynolds numbers of 200 000 and 400 000 is observable for the negative AoA especially for the moment polar plot (see Fig. 14b): At the Reynolds number of 200 000 and negative AoA, the artificial glaze ice induced higher drag penalties and a more negative moment coefficient.

A comparison of the stated Reynolds number independence to Bragg et al. [6, p. 356] points out a similarity: Bragg et al. stated a minor influence of the Reynolds number on the aerodynamic performance of iced airfoils, since the boundary-layer separation is dominated by the ice shape topology and location and less dependant on the Reynolds number as it is the case for clean airfoils [6, p. 356]. This seems to be also applicable on the tested one order of magnitude lower Reynolds number regimes for positive AoA as Fig. 14 shows.

Limitations of the Spalart-Allmaras turbulence model at low Reynolds numbers The analysis of the aerodynamic penalties and comparison of the experimental and numerical results revealed the limitations of the FENSAP module and the chosen Spalart-Allmaras turbulence model. These were partly situated in the prediction of the maximum lift and stall behaviour of the clean airfoil, which was in general more conservative at the Reynolds numbers of 200 000 and 400 000. However, the experimentally observed minor effect of the Reynolds number regime on the aerodynamic performance of the glaze iced RG-15 at positive AoA was captured by the CFD simulations. It turned out that the Spalart-Allmaras turbulence model has deficiencies in the glaze ice case regarding the prediction of the pressure coefficient distribution, but it is able to reasonable capture the characteristics of the drag polar.

This relatively poor agreement of the pressure distribution after a glaze-ice like shape between the experiments and the numerical simulations with the Spalart-Allmaras turbulence model was also pointed out in literature by Chung and Addy [27]. They evaluated amongst other things the performance of different turbulence models like the Spalart-Allmaras turbulence model in numerical iced airfoil simulations.

Also according to Schwarze [32, p. 147], an one-equation turbulence model like the Spalart-Allmaras is rather inadequate for the modulation of complex, more generalized airflows. Schwarze [32, p. 152] mentions on this topic that especially highly 3D flow fields with upstream and tangential directed pressure gradients are problematic for the approach to use a high Reynolds number turbulence model with a wall function for simulating low Reynolds number flow fields.

This is why it was concluded, that higher order turbulence models, such as Reynolds stress and non-linear eddy viscosity models, might be more suitable for predicting the ice-induced aerodynamic penalties of typical UAV airfoils

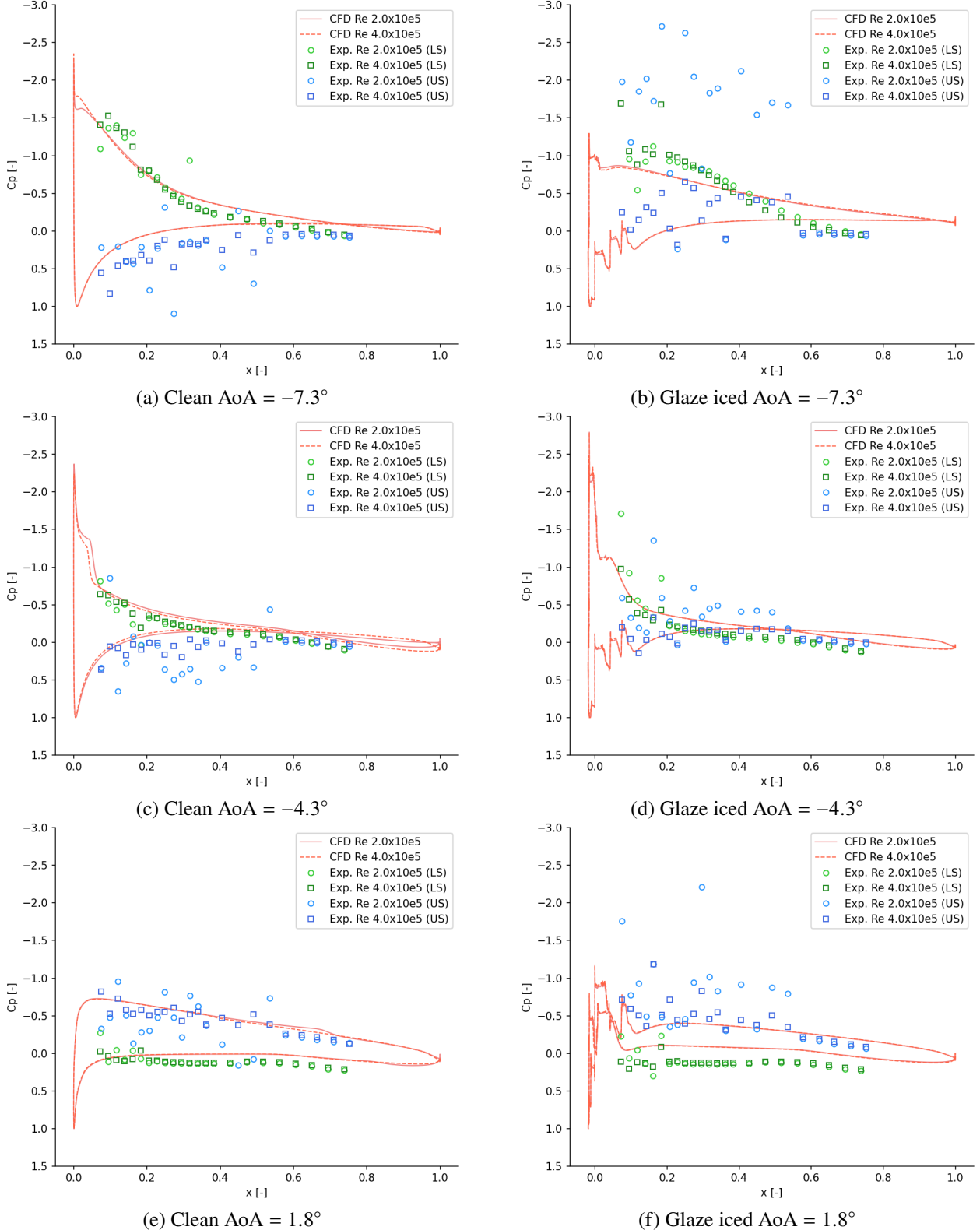
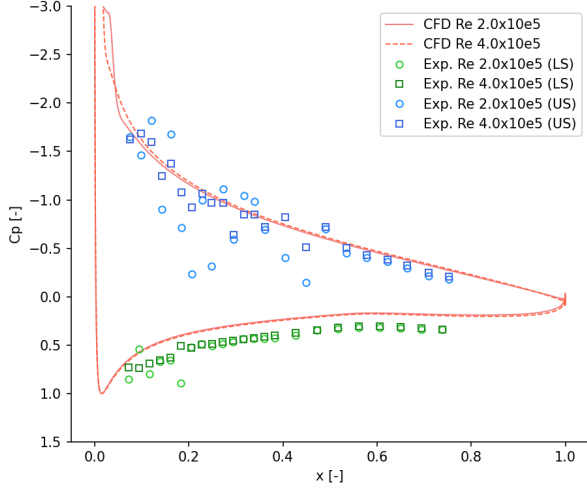
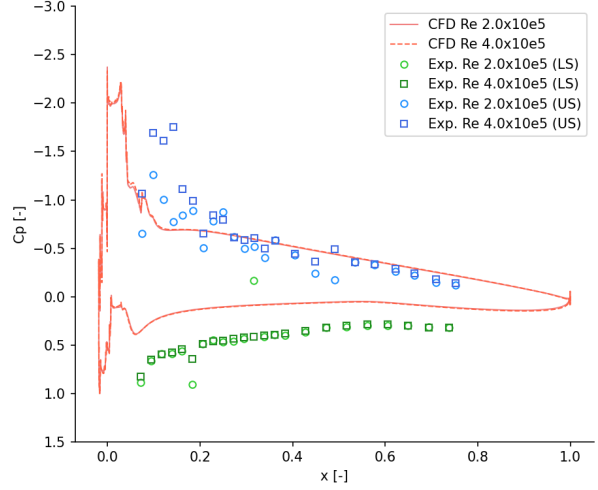


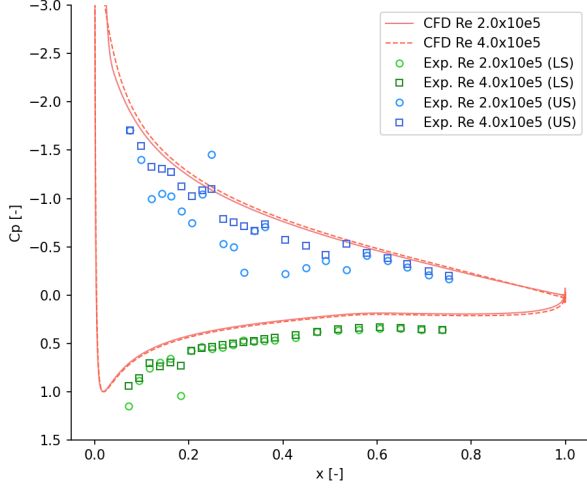
Fig. 12 Clean (left column) and glaze iced (right column) airfoil pressure coefficient c_p over dimensionless chord location x at multiple AoA. Displayed are each the FENSAP clean RG-15C predictions in red, the experiments' upper airfoil side (US) pressure coefficient c_p in blue and the experiments' lower airfoil side (LS) pressure coefficient c_p in green colours.



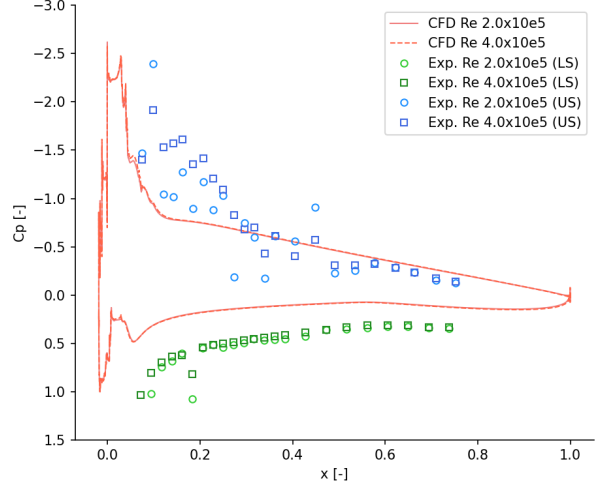
(a) Clean AoA = 7.8°



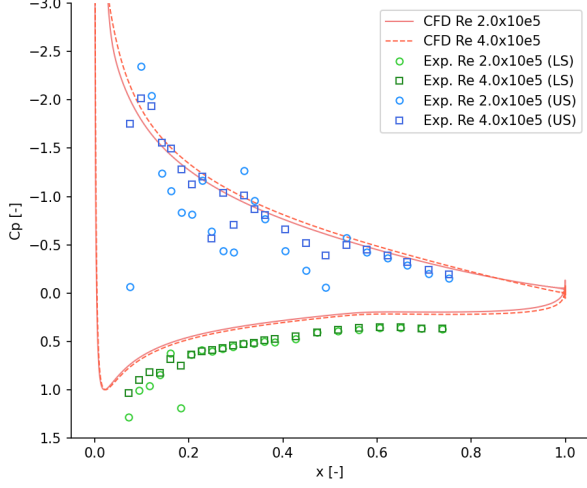
(b) Glaze iced AoA = 7.8°



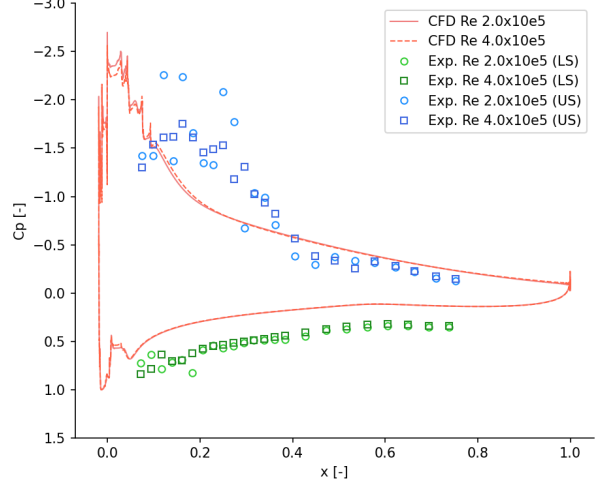
(c) Clean AoA = 8.8°



(d) Glaze iced AoA = 7.8°



(e) Clean AoA = 9.8°



(f) Glaze iced AoA = 9.8°

Fig. 13 Clean (left column) and glaze iced (right column) airfoil pressure coefficient c_p over dimensionless chord location x at multiple positive AoA. Displayed are each the FENSAP RG-15C predictions in red, the experiments' upper airfoil side (US) pressure coefficient c_p in blue and the experiments' lower airfoil side (LS) pressure coefficient c_p in green colours.

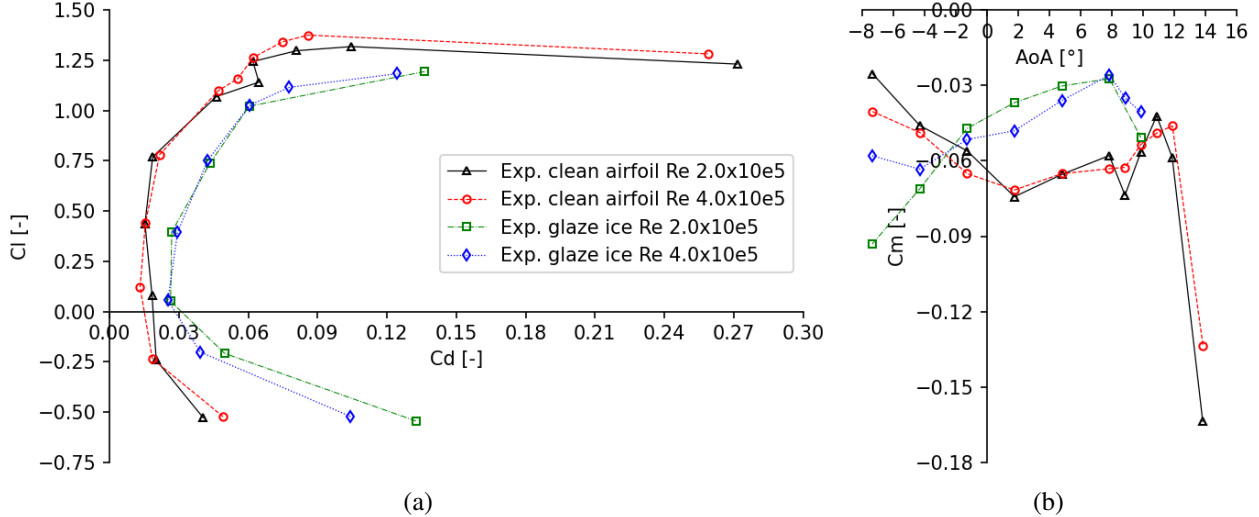


Fig. 14 Comparison of the experimental aerodynamic coefficient results at multiple Reynolds number regimes with lift coefficient c_l over drag coefficient c_d (a) and moment coefficient c_m over angle of attack AoA (b) polar plots. The plots indicate a minor influence of the Reynolds number on the aerodynamic performance of the artificial glaze iced and clean RG-15 at positive AoA.

at low Reynolds number regimes. Readdressing Chang and Addy's [27] studies on numerical predictions of an iced NLF-0414, they also suggested further investigations on turbulence models to determine which are the best performing ones for different ice shapes.

Clean airfoil rapid drag level raise All clean airfoil polar plots obtained experimentally exhibited a higher drag level compared to the CFD simulations and available literature data like Selig [15] or Sartorius [29]. Additionally, a rapid drag increase starting from $AoA > 4.8^\circ$ was observed as well. For example, at the Reynolds number of 200 000 at the $AoA = 9^\circ$, the experimental drag coefficients were up to 90% higher than the literature experimental data and up to 130% higher than the CFD simulations. However, the affected region $4.8^\circ < AoA < 10.8^\circ$ shows regarding the pressure distribution a good agreement between the CFD simulations and the conducted experiments (see Fig. 13a, c, e). The pressure taps were located half-span of the wind tunnel wing model and therefore barely affected by 3D flow effects introduced by e.g. the gap between wooden side walls and the wing model. This is why it was concluded that the observed rapid drag increase was introduced by 3D effects located at the wing model tips.

The work of Barber [33] encouraged this conclusion. Barber investigated intersection losses at the junction of a planar side wall and a symmetric airfoil at low Reynolds numbers. He observed an horseshoe vortex to arise at the junction. Furthermore, Barber found that the produced losses are strongly dependant on the initial boundary layer thickness at the blunt protuberance of the airfoil leading edge. The losses are mainly reflected at low speed flows in form of additional drag caused by the onset of a separation zone at the rear airfoil junction with the side wall [34].

Since no flow visualization techniques or boundary layer measurements were conducted, making a statement on the flow distortion at the junction was difficult. In conclusion, the increased drag level and rapid drag increase at higher AoA was correlated phenomenologically to the distortion of the 2D-flow over the airfoil near the junction of the airfoil and the side wall, which was most likely induced by the interaction between the side wall's boundary layer and the airfoil leading edge.

V. Conclusion

Experimental and numerical studies on the aerodynamic impact of atmospheric in-flight icing at low Reynolds numbers of a typical fixed-wing and medium sized UAV type airfoil were conducted throughout this paper. The studies were motivated by the lack of available experimental data on the aerodynamic icing penalties at low Reynolds numbers on typical UAV airfoils. Existing numerical tools are validated for Reynolds numbers, which are typically one order of magnitude higher than those of the mentioned UAV type. To enable the development of ice-protection technologies also

for UAV applications, the existing numerical tools must be validated for the low Reynolds number regimes of these UAV applications. This is why, this paper aimed to contribute to the validation process of the FENSAP module with experimental data on the aerodynamic penalties of a typical and glaze iced UAV airfoil.

The experimental campaign was conducted inside the large L1-B wind tunnel of the VKI at the Reynolds numbers of 200 000 and 400 000. The utilized wing model was based on the standard radio controlled model sailplane RG-15 airfoil and had a chord length of 450 mm. The RG-15 wind tunnel wing model was artificially glaze iced by adding a 3D-printed ice geometry to the leading edge of the wing model and angular sweeps were performed.

The experimental campaign revealed the glaze ice shape to introduce significant aerodynamic penalties to the RG-15 wind tunnel wing model. The glaze ice shape introduced in general an unstable "nose-down" moment coefficient to the clean RG-15 wind tunnel wing model. For positive AoA, the aerodynamic performance of the glaze iced RG-15 airfoil showed no significant dependency on the Reynolds number. All clean airfoil experiments exhibited rapid drag level increases for $AoA > 4.8^\circ$ and showed an higher drag level compared to literature data at a Reynolds number of 200 000 and the FENSAP CFD simulations in general. This was correlated to the interaction between the wind tunnel side wall boundary layer and the airfoil leading edge at the junction of the airfoil and the side wall.

The numerical campaign was conducted with the FENSAP flow solver module of ANSYS FENSAP-ICE and the one-equation Spalart-Allmaras turbulence model. The flow transition locations of the clean RG-15C were predicted by the software tool XFOIL and prescribed to the steady-state 2D RANS CFD simulations. It was assumed for the iced RG-15C airfoil that the flow transition is triggered by the ice accretion. The reference conditions of the FENSAP CFD simulations were adapted from the experimental campaign ambient conditions.

The numerical simulation approach showed limitations in the prediction of the maximum lift and stall behaviour of the clean RG-15C airfoil, which was in general more conservative. The drag coefficient of the RG-15 wind tunnel wing model was in general under-predicted but was also suspected to be contaminated by the mentioned interaction between the side wall boundary layer and the airfoil. The drag coefficients of the simulated and experimental glaze ice case were fairly matching but also under-predicted. The simulations showed deficiencies in the glaze ice case regarding the pressure coefficient distribution at AoA near the onset of stall. Combined with results from literature this led to the conclusion that the Spalart-Allmaras turbulence model seemed to be limited applicable for estimating the ice induced aerodynamic penalties at low Reynolds numbers. To justify this conclusion, further experiments must be conducted with improvements of the experimental methodological approach.

It is recommended to conduct more aerodynamic experiments with other ice shapes from e.g. rime and mixed ice accretion conditions. Furthermore, the investigation of other turbulence models of higher order such as Reynolds stress and non-linear eddy viscosity models is also recommended for the numerical simulations. Especially the inclusion of flow visualization techniques like particle image velocimetry would allow a cross-validation of the numerical and experimental flow fields.

VI. Contributions

Conceptualization, R.H.; Methodology, J.W.O., A.E., R.H., G.G.; Software, J.W.O. and R.H.; Validation, J.W.O., A.E., R.H.; Formal Analysis, J.W.O.; Investigation, J.W.O., A.E., R.H., and G.G.; Resources, A.E. and R.H.; Data Curation, J.W.O.; Writing – Original Draft Preparation, J.W.O.; Writing – Review and Editing, all; Visualization, J.W.O.; Supervision, A.E., R.H., T.L.; Project Administration, A.E., R.H.; Funding Acquisition, J.W.O. and R.H.

VII. Acknowledgments

The authors thank the NTNU for providing the wing, the ice shape data, and the access to the numerical tools. The authors thank the VKI for providing the testing time in the facility, instrumentation, and technical support.

The work is partly sponsored by the Research Council of Norway through the Centre of Excellence funding scheme, project number 223254, AMOS and project number 269228, BIA Rotors. Numerical simulations were performed with resources from UNINETT Sigma2 under project code NN9613K Notur/NorStore.

A. Enache gratefully acknowledges the Belgian F.R.S.-FNRS for their support with a FRIA fellowship - grant number 35484427.

This work was done with the support of the Erasmus+ programme of the European Union.

References

- [1] Federal Aviation Administration, “FAA Aerospace Forecast Fiscal Years 2019-2039,” research report, USA, 2019.
- [2] QY Research, “Global Commercial Drones Market Report, History and Forecast 2014-2025, Breakdown Data by Manufacturers, Key Regions, Types and Application,” market report 1140178, 2019. URL <https://www.qyresearch.com/index/detail/1140178/global-commercial-drones-market>.
- [3] Shakhatreh, H., Sawalmeh, A. H., Al-Fuqaha, A., Dou, Z., Almaita, E., Khalil, I., Othman, N. S., Khereishah, A., and Guizani, M., “Unmanned Aerial Vehicles (UAVs): A Survey on Civil Applications and Key Research Challenges,” *IEEE Access*, Vol. 7, 2019, pp. 48572–48634. <https://doi.org/10.1109/ACCESS.2019.2909530>.
- [4] Hann, R., and Johansen, T. A., “Unsettled Topics in Unmanned Aerial Vehicle Icing,” SAE EDGE research report EPR2020008, 2020. <https://doi.org/10.4271/EPR2020008>.
- [5] Hann, R., “Atmospheric Ice Accretions, Aerodynamic Icing Penalties, and Ice Protection Systems on Unmanned Aerial Vehicles,” Phd thesis ntnu2020:200, Norwegian University of Science and Technology, 2020.
- [6] Bragg, M. B., Broeren, A. P., and Blumenthal, L. A., “Iced-airfoil aerodynamics,” *Progress in Aerospace Sciences*, Vol. 41, No. 5, 2005, pp. 323–362. <https://doi.org/10.1016/j.paerosci.2005.07.001>.
- [7] Sørensen, K. L., Borup, K. T., Hann, R., Bernstein, B. C., and Hansbø, M., “UAV Atmospheric Icing Limitations,” research report, retrieved 1 November 2021. URL <https://www.ubiquaerospace.com/climate-report>.
- [8] Hann, R., “UAV Icing: Ice Accretion Experiments and Validation,” *SAE Technical Paper Series, No. 2019-01-2037*, SAE International, 2019. <https://doi.org/10.4271/2019-01-2037>.
- [9] Pretz, K., “UBIQ Aerospace Brings the First Drone De-Icing System to Market,” *IEEE Spectrum*, accessed 23 November 2021. URL <https://spectrum.ieee.org/the-institute/ieee-member-news/ubiq-aerospace-brings-the-first-drone-deicing-system-to-market>.
- [10] Szilder, K., and McIlwain, S., “In-Flight Icing of UAVs - The Influence of Reynolds Number on the Ice Accretion Process,” *SAE Technical Paper Series*, SAE International, 2011. <https://doi.org/10.4271/2011-01-2572>.
- [11] Williams, N., Benmeddour, A., Brian, G., and Ol, M., “The effect of icing on small unmanned aircraft low Reynolds number airfoils,” *AIAC 2017*, 17th Australian International Aerospace Congress, Melbourne, Australia, 2017.
- [12] Szilder, K., and Yuan, W., “In-flight icing on unmanned aerial vehicle and its aerodynamic penalties,” *Progress in Flight Physics*, Vol. 9, EDP Sciences, 2017, pp. 173–188. <https://doi.org/10.1051/eucass/2016090173>.
- [13] Fajt, N., Hann, R., and Lutz, T., “The Influence of Meteorological Conditions on the Icing Performance Penalties on a UAV Airfoil,” Proceedings of the 8th European Conference for Aeronautics and Space Sciences, Madrid, Spain, 2019. <https://doi.org/10.13009/EUCASS2019-240>.
- [14] Coudou, N., “WIND TURBINE / FARM WAKE(S) MEANDERING STUDY IN AN ABL WIND TUNNEL,” research report 2016-05, von Karman Institute for Fluid Dynamics, Rhode Saint Genèse, Belgium, 2016.
- [15] Selig, M., Guglielmo, J., Broeren, A., and Giguère, P., *Summary of Low-Speed Airfoil Data*, 1st ed., SoarTech Publications, Virginia Beach, Virginia, USA, 1995.
- [16] Maritime Robotics AS, “THE FALK,” accessed 27 November 2021. URL <https://www.maritimerobotics.com/falk>.
- [17] Selig, M., “UIUC Applied Aerodynamics Group Department of Aerospace Engineering,” retrieved 8 January 2021. URL https://m-selig.ae.illinois.edu/ads/coord_database.html.
- [18] xflr5 v6.48, “xflr5, General description,” accessed 20 March 2021. URL <http://www.xflr5.tech/xflr5.htm>.
- [19] Jokela, T., and Prieto, R., “Icing wind tunnel,” retrieved 11 February 2021. URL https://www.vttresearch.com/sites/default/files/2020-06/Wind%20power_Icing_wind_tunnel.pdf.
- [20] Oswald, J. W., “UAV Icing: Numerical and Experimental Study of Performance Penalties on an RG-15 Airfoil,” master thesis, University of Stuttgart, 2021. URL https://folk.ntnu.no/richahan/Publications/2021_Oswald_Thesis.pdf.
- [21] Morris, A. S., and Langari, R., *Measurement and Instrumentation*, 1st ed., Elsevier Inc., San Diego, California, USA, 2012.

- [22] Barlow, J. B., W. H. Rae, J., and Pope, A., *LOW-SPEED WIND TUNNEL TESTING*, 3rd ed., John Wiley and Sons Inc., USA, 1999.
- [23] Allen, H. J., and Vincenti, W. G., “Wall interference in a two-dimensional-flow wind tunnel, with consideration of the effect of compressibility,” report NACA-TR-782, NASA, 1944. URL <https://ntrs.nasa.gov/citations/19930091861>.
- [24] Ansys, Inc, “Ansys FENSAP-ICE, Ice Accretion Simulation Software,” accessed 21 Mai 2021. URL <https://www.ansys.com/products/fluids/ansys-fensap-ice>.
- [25] Baruzzi, G. S., Habashi, W. G., Guèvremont, G., and Hafez, M. M., “A Second Order Finite Element Method for the Solution of the Transonic Euler and Navier-Stokes Equations,” *International Journal for Numerical Methods in Fluids*, Vol. 20, No. 8, 1995, pp. 671–693. <https://doi.org/10.1002/fld.1650200802>.
- [26] Pointwise, “Mesh and Grid Generation Software for CFD,” accessed 21 Mai 2021. URL <https://www.pointwise.com/pointwise-software>.
- [27] Chung, J., and H. Addy, J., “A numerical evaluation of icing effects on a natural laminar flow airfoil,” AIAA, 38th Aerospace Sciences Meeting and Exhibit, Reno, Nevada, USA, 2000. <https://doi.org/10.2514/6.2000-96>.
- [28] Drela, M., “XFOIL: An Analysis and Design System for Low Reynolds Number Airfoils,” *Low Reynolds Number Aerodynamics*, Lecture Notes in Engineering, Vol. 54, edited by T. J. Mueller, Springer, 1989, pp. 1–12. https://doi.org/10.1007/978-3-642-84010-4_1.
- [29] Sartorius, D., “Hitzdrahtmessungen zur Grenzschicht- und Nachlaufentwicklung bei Ablöseblasen in der Nähe der Profilhinterkante,” Diplomarbeit, Institut für Aerodynamik und Gasdynamik, Universität Stuttgart, 2001.
- [30] Lutz, T., Würz, W., and Wagner, S., “Numerical Optimization and Wind-Tunnel Testing of Low Reynolds-Number Airfoils,” *Proceedings Conference on: Fixed, Flapping and Rotary Wing Vehicles At Very Low Reynolds Numbers*, University of Notre Dame, Indiana, USA, 2000.
- [31] O’Meara, M. M., and Mueller, T. J., “Laminar Separation Bubble Characteristics on an Airfoil at Low Reynolds Numbers,” *American Institute of Aeronautics and Astronautics (AIAA) Journal*, Vol. 25, No. 8, 1987, pp. 1033–1041. <https://doi.org/10.2514/3.9739>.
- [32] Schwarze, R., *CFD-Modellierung*, 1st ed., Springer, 2013. <https://doi.org/10.1007/978-3-642-24378-3>.
- [33] Barber, T. J., “An Investigation of Strut-Wall Intersection Losses,” *Journal of Aircraft*, Vol. 15, No. 10, 1978, pp. 676–681. <https://doi.org/10.2514/3.58427>.
- [34] Mokry, M., Chan, Y. Y., and Jones, D. J., *Two-dimensional Wind Tunnel Wall Interference*, 7th ed., Advisory Group for Aerospace Research and Development, North Atlantic Treaty Organization, Neuilly sur Seine, France, 1983.